# The 1.4-GHz radio properties of hard X-ray-selected AGN

F. Panessa,[1]★ A. Tarchi,[2] P. Castangia,[2] E. Maiorano,[3] L. Bassani,[3] G. Bicknell,[4] A. Bazzano,[1] A. J. Bird,[5] A. Malizia[3] and P. Ubertini[1]

[1]*INAF – Istituto di Astrofisica e Planetologia Spaziali di Roma (IAPS), Via del Fosso del Cavaliere 100, I-00133 Roma, Italy*
[2]*Osservatorio Astronomico di Cagliari (OAC-INAF),Via della Scienza 5, I-09047 Selargius (CA), Italy*
[3]*Istituto di Astrofisica Spaziale e Fisica Cosmica (IASF-INAF), Via P. Gobetti 101, I-40129 Bologna, Italy*
[4]*Research School of Astronomy & Astrophysics, Mt Stromlo Observatory, Cotter Rd, Weston, ACT 2611, Australia*
[5]*Physics & Astronomy, University of Southampton, Highfield, Southampton SO17 1BJ, UK*

## ABSTRACT

We have analysed the NRAO Very Large Array Sky Survey and Sydney University Molonglo Sky Survey data at 1.4 GHz and 843 MHz for a well-defined complete sample of hard X-ray AGN observed by *INTEGRAL*. A large number (70/79) of sources are detected in the radio band, showing a wide range of radio morphologies, from unresolved or slightly resolved cores to extended emission over several hundreds of kpc scales. The radio fluxes have been correlated with the 2–10 keV and 20–100 keV emission, revealing significant correlations with slopes consistent with those expected for radiatively efficient accreting systems. The high-energy emission coming from the inner accretion regions correlates with the radio emission averaged over hundreds of kpc scales (i.e. thousands of years).

**Key words:** galaxies: active – galaxies: Seyfert – radio continuum: galaxies.

## 1 INTRODUCTION

How active galactic nuclei (AGN) are involved in the process of galaxy formation is one of the main issues in modern astrophysics. AGN and galaxy evolution are connected through feedback processes regulating both the accretion history and the star formation (e.g. Cattaneo et al. 2009). The mechanical (kinetic) energy released by accelerated particles in jets is one of the possible sources of AGN feedback into the interstellar matter of the host galaxy (Cattaneo et al. 2006; Croton et al. 2006; Marulli et al. 2008). The knowledge of the connection between the radio emission (linked to the jet) and the X-ray emission (from accretion) is one of the key ingredients to build up more robust AGN-galaxy evolutionary models (La Franca, Melini & Fiore 2010; Bonchi et al. 2013). The X-ray versus radio connection is also fundamental within the disc–jet coupling paradigm in accreting systems (Merloni, Heinz & di 2003; Falcke, Körding & Markoff 2004). However, the details of the link between the accreting disc, the X-ray corona and the jet are still under investigation.

The relation between the radio and the X-ray emission has been explored for different classes of AGN, with correlation slopes typically distributed around unity (Canosa et al. 1999; Brinkmann et al. 2000; Panessa et al. 2007). The discovery of a 'Fundamental Plane' relation between the X-ray and radio luminosities, and the black hole (BH) mass (Merloni et al. 2003; Falcke et al. 2004) has been interpreted in the framework of a radiatively inefficient accretion flow accompanied by a relativistic jet at work both in X-ray binaries (XRBs) and low-luminosity AGN (e.g. Narayan & Yi 1994). Recently, Coriat et al. (2011) have shown that some XRBs follow a steeper radio–X-ray correlation (correlation slope of 1.4) compared to the standard 0.5–0.7 (Gallo, Fender & Pooley 2003; Merloni et al. 2003), suggesting that these sources are accreting at high Eddington ratios and are radiatively efficient. Dong, Wu & Cao (2014) have confirmed this result for a sample of bright radiatively efficient AGN, with a positive correlation slope of ∼1.6, justified within the disc–corona model for efficient accreting sources (e.g. Cao, Wu & Dong 2014). On the other hand, Burlon et al. (2013) have explored the association between hard X-ray AGN observed by *Swift*/BAT and AT20G[1] radio sources in the southern sky, finding a possible correlation between the 15–55 keV and 20 GHz luminosities (slope of ∼0.7), however, likely driven by distances effects and therefore not intrinsically significant.

Here, we aim at testing the validity of such correlations in a well-defined complete sample of relatively high-luminosity AGN, selected at hard X-ray as those observed by the *INTEGRAL* satellite (e.g. Bird et al. 2010). *INTEGRAL*/IBIS is surveying the sky above 20 keV with a sensitivity better than a few mCrab[2] and a point source location accuracy of 1–3 arcmin depending on the

---

[1] The AT20G Survey is a blind 20 GHz survey of the entire southern sky carried out using the Australia Telescope Compact Array (ATCA).
[2] The conversion factor in the 20–40 keV range is 10 mCrab = 7.57 × $10^{-11}$ erg cm$^{-2}$ s$^{-1}$; see Bird et al. (2010).

★E-mail: francesca.panessa@iaps.inaf.it

source significance and the observation exposure (Bird et al. 2007). Hard X-ray-selected samples are almost unbiased with respect to absorption and are mostly located in the nearby Universe, reducing as much as possible the selection effects (Malizia et al. 2009). The sample used here comprises bright AGN ($41.5 < L_{2-10\,keV} < 44.5$ in erg s$^{-1}$), with Eddington ratios $L_{bol}/L_{Edd} \geq 10^{-3}$, good candidates for radiating at efficient accretion regimes.

In Section 2, we present the *INTEGRAL* sample and the treatment of the X-ray data; in Sections 3 and 4, we describe the radio data analysis and the radio properties of the sample; in Section 5, the radio versus X-ray correlation statistical results are presented; in Sections 6 and 7, we report our discussion and conclusions. Throughout this paper, we assume a flat $\Lambda$ cold dark matter cosmology with $(\Omega_M, \Omega_\Lambda) = (0.3, 0.7)$ and a Hubble constant of 70 km s$^{-1}$ Mpc$^{-1}$ (Jarosik et al. 2011).

## 2 THE SAMPLE AND THE X-RAY DATA

The sample is extracted from the third *INTEGRAL*/IBIS survey which lists around 140 (identified and candidates) AGN (Bird et al. 2007). To this large sample, the $V/V_{max}$ test[3] has been applied to obtain a complete sample of 79 AGN selected in the hard (20–40 keV) X-ray band above ~5$\sigma$ confidence level (see Malizia et al. 2009 for the detailed definition of the method and sample); the sample includes 46 Seyfert 1 (including 6 narrow-line objects) and 33 Seyfert 2. The original sample in Malizia et al. (2009) contains also nine blazars, which we have excluded in the present study because Doppler boosting effects prevent from a correct determination of the intrinsic radio luminosity.

The X-ray properties of the sample are described in Malizia et al. (2009) where the 20–100 keV fluxes were taken from the *INTEGRAL* survey (Bird et al. 2007), while the 2–10 keV observed fluxes and column densities were collected from the literature. In order to obtain the 2–10 keV unabsorbed fluxes from the observed ones, we have here applied a correction factor proportional to the measured X-ray column density $N_H$ as in column 8 of table 1 in Malizia et al. (2009), assuming simple photoelectric absorption in XSPEC. The sample includes five Compton thick AGN (MKN 3, NGC 3281, NGC 4945, Circinus galaxy, IGR J16351−5806 and NGC 1068), for which both 2–10 and 20–100 keV fluxes require a correction (the hard X-ray fluxes are very marginally affected by absorption for $N_H < 10^{24}$ cm$^{-2}$). In Malizia et al. (2009), the correction in the 20–40 keV flux as a function of $N_H$ was calculated using a simple absorbed power-law model in XSPEC, obtaining an average flux reduction negligible below log $N_H = 24$ and progressively more important thereafter (8, 25 and 64 per cent reduction in the ranges 24–24.5, 24.5–25 and 25–25.5, respectively). In Burlon et al. (2011), the observed/intrinsic flux ratio is plotted against the $N_H$ value, a few Compton thick sources with available observed and intrinsic luminosities are overplotted to the predicted trend for local AGN. The flux reduction is 40, 85 and 94 per cent in the ranges 24–24.5, 24.5–25 and 25–25.5, respectively. In this work, we have applied a tentative flux correction as in Burlon et al. (2011). We should also consider that for the heavily absorbed source NGC

1068 ($N_H > 10^{25}$ cm$^{-2}$), an estimate of the intrinsic hard luminosity is difficult to obtain, given its spectral complexity and the unknown precise value of $N_H$ (Iwasawa, Fabian & Matt 1997; Matt et al. 2004).

## 3 THE RADIO DATA

The NRAO VLA Sky Survey (NVSS; Condon et al. 1998) is a 1.4 GHz continuum survey covering the entire sky north of −40 deg declination. The restoring beam of the NVSS maps is 45 arcsec full width at half-maximum (FWHM) and the rms brightness fluctuations in the images are about 0.45 mJy beam$^{-1}$. The Sydney University Molonglo Sky Survey (SUMSS; Bock, Large & Sadler 1999; Mauch et al. 2003) at 843 MHz covers the whole sky south of declination −30 deg and produces images with a resolution of 45 arcsec × 45 arcsec cosec |dec| and an rms noise level of ~1 mJy beam$^{-1}$. Thus, SUMSS and NVSS have similar sensitivity and resolution, and together cover the whole sky.

We extracted maps of about 30 arcmin × 30 arcmin in size from the Postage Stamp Services available for both surveys centring the requested map at the coordinates of the optical nucleus of the galaxy associated by Malizia et al. (2009) to the *INTEGRAL* source. FITS images were imported into NRAO Astronomical Image Processing System (AIPS) and analysed using standard AIPS tasks. When the radio sources are either unresolved or slightly resolved, all parameters and associated errors were determined through a Gaussian fit of each component using the AIPS task IMFIT. For extended sources, coordinates and flux density of the radio emission peaks were obtained using the AIPS task TVSTAT. The integrated flux density were also obtained using TVSTAT over a polygon encompassing the radio emission visible down to the 3$\sigma$ level of the map to avoid confusion with the extended background emission.

The measured quantities are collected in Table 1.

For unresolved sources, i.e. those for which IMFIT computes FWHM values smaller than one-half the restoring beam[4] size in both dimensions, the reported sizes are set to one-half the restoring beam size at FWHM. These dimensions are obviously upper limits because the true dimensions are not known. We define slightly resolved sources as those for which IMFIT computes values for the size larger than one-half the restoring beam size at FWHM in at least one of the two dimensions. In this case, the reported angular size is the deconvolved size provided by IMFIT for the slightly-resolved dimension(s) and one-half the restoring beam size at FWHM, otherwise. For those sources marked as resolved, namely those for which fitting the emission with a single Gaussian was clearly not suitable, the extension of the radio source has been computed directly from the map by measuring the extension of the radio emission visible above a 3$\sigma$ level in two orthogonal directions. Note that the different frequency between the two surveys does not allow a direct comparison of the linear dimensions, different radio structures are indeed detected depending on the observational frequency. The errors on the estimated quantities were directly provided by the task IMFIT (when used). For the extended sources, we decided to use the noise of the map (determined from a source-free rectangular region) as the uncertainty on the peak flux density, while the uncertainty on

---

[3] A test of the uniformity of the space distribution in a flux-limited sample is introduced by Schmidt (1968). The test compares the volume ($V$) enclosed within the distance of a source with the maximum volume ($V_{max}$) that would be enclosed at the maximum redshift at which the object would be detectable.

[4] The restoring beam size of the NVSS and SUMSS images is 45 arcsec × 45 arcsec and 43 arcsec × 43 arcsec, respectively.

the integrated flux density was computed using the formula

$$\Delta S_i = \sigma \times \sqrt[2]{\frac{\mathrm{pix_{area}}}{\mathrm{pix_{beam}}}},$$

where $\sigma$ is the rms noise, $\mathrm{pix_{area}}$ and $\mathrm{pix_{beam}}$ are the number of pixel within the area over which we integrate and the pixel in the beam, respectively.

For the SUMSS sources, the flux density at 843 MHz has been converted into 1.4-GHz flux density assuming $S_\nu \propto \nu_{-\alpha}$ with

**Table 1.** The NVSS data for the *INTEGRAL*/IBIS complete sample of AGN.

| Name (1) | Class (2) | $z$ (3) | $L_{\mathrm{X}}$ (4) | $L_{\mathrm{HX}}$ (5) | $S_{\mathrm{p}}$ (6) | $S_{\mathrm{i}}$ (7) | $L_{\mathrm{p}}$ (8) | $L_{\mathrm{i}}$ (9) | $D_{\mathrm{min}}$ (10) | $D_{\mathrm{maj}}$ (11) | Mor. (12) | $M$ (13) | Ref. (14) |
|---|---|---|---|---|---|---|---|---|---|---|---|---|---|
| IGR J00333+6122 | Sy 1.5 | 0.1050 | 44.19 | 44.44 | 9.0 | 9.5 | 39.46 | 39.48 | < 49.09 | < 49.09 | U | 8.5 | 1 |
| NGC 788 | Sy 2 | 0.0136 | 42.86 | 43.29 | 6.0 | 19.5 | 37.61 | 38.17 | 27.13 | 35.6 | R | 7.5 | 2 |
| NGC 1068 | Sy 2 | 0.0038 | 42.95 | 43.35 | 4.5e3 | 5.0e3 | 39.27 | 39.32 | 17.05 | 18.95 | R | 7.2 | 2 |
| QSO B0241+62 | Sy 1 | 0.0440 | 43.87 | 44.41 | 353.8 | 374.9 | 40.30 | 40.32 | < 20.57 | < 20.57 | U | 8.5 | 3 |
| NGC 1142 | Sy 2 | 0.0288 | 43.82 | 43.96 | 139.5 | 158.4 | 39.53 | 39.58 | < 13.46 | < 13.46 | U | 9.4 | 2 |
| B3 0309+411B | Sy 1 | 0.1360 | 45.04 | 44.99 | 344.8 | 389.5 | 41.27 | 41.44 | 423.9 | 1373 | R | – | – |
| NGC 1275 | Sy 2 | 0.0175 | 42.89 | 43.38 | 2.3e4 | 2.3e4 | 41.30 | 41.33 | 93.81 | 109.1 | R | 8.5 | 2 |
| 3C 111 | Sy 1 | 0.0485 | 44.52 | 44.66 | 3.5 | 15.1 | 41.38 | 42.01 | 320.5 | 393 | R | 9.6 | 2 |
| LEDA 168563 | Sy 1 | 0.0290 | 43.90 | 44.04 | 12.4 | 15.0 | 38.48 | 38.56 | < 13.56 | 15.68 | S | 8.0 | 4 |
| 4U 0517+17 | Sy 1.5 | 0.0179 | 43.23 | 43.62 | 6.0 | 6.1 | 37.75 | 37.76 | < 8.368 | 8.484 | S | 7.0 | 5 |
| MCG+08-11-11 | Sy 1.5 | 0.0205 | 43.69 | 43.74 | 228.5 | 249.3 | 39.45 | 39.50 | 38.33 | 84.34 | R | 8.1 | 2 |
| Mrk 3 | Sy 2 | 0.0135 | 44.17 | 43.79 | 1.1e3 | 1.1e3 | 39.76 | 39.77 | < 6.311 | < 6.311 | U | 8.7 | 2 |
| Mrk 6 | Sy 1.5 | 0.0188 | 43.27 | 43.57 | 259.6 | 281.2 | 39.43 | 39.46 | < 8.789 | < 8.789 | U | 8.2 | 2 |
| IGR J07565−4139 | Sy 2 | 0.0210 | 42.14 | 43.21 | 5.4 | 3.9 | 37.84 | 37.70 | < 9.381 | 14.05 | S* | – | – |
| IGR J07597−3842 | Sy 1.2 | 0.0400 | 43.90 | 44.11 | 3.8 | 3.6 | 38.24 | 38.22 | < 18.7 | < 18.7 | U | 8.3 | 1 |
| ESO 209−12 | Sy 1 | 0.0396 | 43.43 | 43.87 | 37.6 | 45.6 | 39.23 | 39.32 | < 17.69 | 36.7 | S* | – | – |
| FRL 1146 | Sy 1.5 | 0.0316 | 43.39 | 43.56 | 13.1 | 21.8 | 38.61 | 38.82 | 63.03 | 94.55 | R | – | – |
| SWIFT J0917.2−6221 | Sy 1 | 0.0573 | 44.17 | 44.17 | 41.4 | 46.1 | 39.60 | 39.64 | < 25.6 | 35.35 | S* | 9.9 | 6 |
| MCG−05-23-16 | Sy 2 | 0.0085 | 43.09 | 43.34 | 14.1 | 14.8 | 37.47 | 37.49 | < 3.974 | < 3.974 | U | 6.3 | 2 |
| IGR J09523−6231 | Sy 1.9 | 0.2520 | 45.28 | 45.22 | 5.6 | 5.0 | 40.02 | 39.97 | < 112.6 | < 112.6 | U* | 7.6 | 2 |
| SWIFT J1009.3−4250 | Sy 2 | 0.0330 | 42.96 | 43.81 | 17.2 | 16.8 | 38.74 | 38.73 | < 14.74 | 28.52 | S* | – | – |
| NGC 3281 | Sy 2 | 0.0115 | 43.68 | 43.35 | 73.1 | 81.6 | 38.45 | 38.50 | < 5.376 | < 5.376 | U | 8.0 | 2 |
| SWIFT J1038.8−4942 | Sy 1.5 | 0.0600 | 44.04 | 44.04 | 3.1 | 2.9 | 38.51 | 38.48 | < 26.8 | 30.67 | S* | – | – |
| IGR J10404−4625 | Sy 2 | 0.2392 | 44.93 | 45.58 | 42.0 | 43.3 | 40.84 | 40.86 | < 106.9 | 204 | S* | – | – |
| NGC 3783 | Sy 1 | 0.0097 | 43.07 | 43.42 | 35.5 | 45.5 | 38.00 | 38.15 | 16.93 | 55.63 | R | 7.5 | 2 |
| IGR J12026−5349 | Sy 2 | 0.0280 | 43.11 | 43.81 | 49.9 | 57.5 | 39.06 | 39.34 | 87.27 | 143.1 | R | – | – |
| NGC 4151 | Sy 1.5 | 0.0033 | 43.05 | 43.16 | 348.9 | 370.7 | 38.04 | 38.07 | < 1.543 | < 1.543 | U | 7.5 | 2 |
| Mrk 50 | Sy 1 | 0.0234 | 43.05 | 43.20 | < 1.5 | – | < 37.37 | – | – | – | – | 7.5 | 7 |
| NGC 4388 | Sy 2 | 0.0084 | 43.00 | 43.54 | 93.5 | 125.5 | 38.29 | 38.48 | 28.27 | 49.22 | R | 7.2 | 2 |
| NGC 4507 | Sy 2 | 0.0118 | 43.08 | 43.70 | 47.6 | 67.1 | 38.28 | 38.43 | < 5.999 | 8.086 | R | 7.6 | 2 |
| LEDA 170194 | Sy 2 | 0.0360 | 43.48 | 44.22 | 35.4 | 40.6 | 39.13 | 39.23 | 76.3 | 130.2 | R | 8.9 | 2 |
| NGC 4593 | Sy 1 | 0.0090 | 42.80 | 43.09 | 4.0 | 8.3 | 37.18 | 37.81 | 15.71 | 35.9 | R | 7.0 | 2 |
| IGR J12415−5750 | Sy 1 | 0.0230 | 42.93 | 43.40 | 15.1 | 16.9 | 38.37 | 38.42 | < 10.27 | 15.83 | S* | 8.0 | 1 |
| NGC 4945 | Sy 2 | 0.0019 | 42.20 | 42.55 | 3.9e3 | 4.5e3 | 38.62 | 38.89 | 10.19 | 27 | R | 6.2 | 2 |
| IGR J13091+1137 | Sy 2 | 0.0251 | 43.44 | 43.77 | < 1.4 | – | < 37.42 | – | – | – | – | 8.6 | 2 |
| IGR J13109−5552 | Sy 1 | 0.0850 | 43.88 | 44.56 | 408.9 | 530.5 | 40.94 | 41.21 | 201.3 | 667.6 | R* | – | – |
| Cen A | Sy 2 | 0.0018 | 42.36 | 42.70 | 6.5e3 | 2.1e4 | 39.35 | 40.53 | 4.264 | 33.66 | R* | 8.0 | 2 |
| MCG−06-30-15 | Sy 1.2 | 0.0077 | 42.63 | 42.76 | < 1.5 | – | < 36.40 | – | – | – | – | 6.7 | 2 |
| NGC 5252 | Sy 2 | 0.0230 | 43.72 | 43.71 | 15.9 | 16.9 | 38.39 | 38.41 | < 10.75 | < 10.75 | U | 9.0 | 2 |
| 4U 1344−60 | Sy 1.5 | 0.0130 | 43.70 | 43.41 | < 9.2 | – | 37.50 | 41.54 | – | – | –* | – | – |
| IC 4329A | Sy 1.2 | 0.0160 | 43.74 | 44.06 | 63.6 | 69.0 | 38.67 | 38.76 | 37.9 | 113.7 | R | 7.0 | 2 |
| Circinus Galaxy | Sy 2 | 0.0014 | 42.39 | 42.15 | 715.3 | 1256.9 | 37.64 | 38.04 | 10.3 | 16.41 | R* | 6.0 | 2 |
| NGC 5506 | Sy 1.9 | 0.0062 | 42.83 | 42.85 | 332.3 | 345.7 | 38.57 | 38.59 | < 2.898 | < 2.898 | U | 6.7 | 2 |
| ESO 511−G030 | Sy 1 | 0.2239 | 45.13 | 45.56 | 8.3 | 14.0 | 40.08 | 40.31 | 118.6 | 224.8 | R | 8.7 | 8 |
| IGR J14515−5542 | Sy 2 | 0.0180 | 42.68 | 43.04 | 16.5 | 16.5 | 38.19 | 38.19 | < 8.041 | 11.79 | S* | – | – |
| IC 4518A | Sy 2 | 0.0163 | 42.83 | 43.09 | 144.3 | 184.2 | 39.05 | 39.33 | 48.77 | 71.12 | R* | 7.5 | 9 |
| IGR J16024−6107 | Sy 2 | 0.0110 | 41.66 | 42.46 | 8.8 | 6.1 | 37.49 | 37.33 | < 4.914 | < 4.914 | U* | – | – |
| IGR J16119−6036 | Sy 1 | 0.0160 | 42.24 | 43.13 | < 4.9 | – | < 37.41 | – | – | – | –* | – | – |
| IGR J16185−5928 | NLS1 | 0.0350 | 43.10 | 43.67 | 4.7 | 5.3 | 38.23 | 38.27 | < 15.64 | 38.04 | A* | 7.4 | 1 |
| IGR J16351−5806 | Sy 2 | 0.0091 | 42.51 | 42.74 | 69.8 | 84.2 | 38.22 | 38.41 | 27.23 | 30.63 | R* | – | – |
| IGR J16385−2057 | NLS1 | 0.0269 | 43.02 | 43.39 | 6.5 | 7.2 | 38.13 | 38.24 | < 12.58 | 15.34 | S | 6.8 | 1 |
| IGR J16426+6536 | NLS1 | 0.3230 | – | 45.97 | < 1.2 | – | < 39.57 | – | – | – | – | 7 | 1 |
| IGR J16482−3036 | Sy 1 | 0.0310 | 43.60 | 43.79 | 2.4 | 7.8 | 37.89 | 38.40 | 57.97 | 112.1 | R | 8.2 | 1 |
| IGR J16558−5203 | Sy 1.2 | 0.0540 | 44.33 | 44.31 | 5.3 | 3.0 | 38.65 | 38.40 | < 24.12 | < 24.12 | U* | 7.9 | 1 |
| NGC 6300 | Sy 2 | 0.0037 | 41.87 | 42.28 | 18.8 | 64.3 | 36.92 | 37.54 | 11.53 | 20.3 | R* | 5.5 | 2 |
| GRS 1734−292 | Sy 1 | 0.0214 | 43.56 | 43.90 | 46.3 | 48.5 | 38.79 | 38.81 | < 10 | < 10 | U | 8.9 | 2 |
| 2E 1739.1−1210 | Sy 1 | 0.0370 | 43.56 | 43.89 | 3.4 | 3.1 | 38.13 | 38.09 | < 17.3 | < 17.3 | U | 8.2 | 1 |

**Table 1** – *continued*

| Name (1) | Class (2) | $z$ (3) | $L_X$ (4) | $L_{HX}$ (5) | $S_p$ (6) | $S_i$ (7) | $L_p$ (8) | $L_i$ (9) | $D_{min}$ (10) | $D_{maj}$ (11) | Mor. (12) | $M$ (13) | Ref. (14) |
|---|---|---|---|---|---|---|---|---|---|---|---|---|---|
| IGR J17488−3253 | Sy 1 | 0.0200 | 43.07 | 43.52 | < 1.2 | – | < 37.14 | – | – | – | – | – | – |
| IGR J17513−2011 | Sy 1.9 | 0.0470 | 43.40 | 44.10 | 1.5 | 1.8 | 37.99 | 38.06 | < 21.97 | 59.68 | A | 6.0 | 2 |
| IGR J18027−1455 | Sy 1 | 0.0350 | 43.23 | 44.04 | 5.7 | 8.4 | 38.51 | 38.87 | 30.54 | 144 | R | – | – |
| IGR J18249−3243 | Sy 1 | 0.3550 | 45.13 | 45.47 | 2.7e3 | 4.1e3 | 43.01 | 43.18 | 1593 | 1770 | R | – | – |
| IGR J18259−0706 | Sy 1 | 0.0370 | 43.19 | 43.66 | 2.7 | 9.6 | 38.66 | 38.89 | 69.19 | 133.8 | R | – | – |
| ESO 103−35 | Sy 2 | 0.0133 | 43.26 | 43.49 | 24.5 | 26.0 | 38.10 | 38.13 | < 5.941 | < 5.941 | U* | 7.1 | 2 |
| 3C 390.3 | Sy 1 | 0.0561 | 44.34 | 44.60 | 4.2e3 | 7.0e3 | 41.61 | 42.02 | 230.8 | 419.6 | R | 8.5 | 2 |
| 2E 1853.7+1534 | Sy 1 | 0.0840 | 44.25 | 44.56 | 3.5 | 3.4 | 38.86 | 38.84 | < 39.27 | < 39.27 | U | 8.2 | 1 |
| IGR J19378−0617 | NLS1 | 0.0106 | 42.91 | 42.64 | 39.3 | 44.0 | 38.11 | 38.16 | < 4.955 | < 4.955 | U | 6.8 | 10 |
| NGC 6814 | Sy 1.5 | 0.0052 | 40.98 | 42.52 | 13.7 | 52.9 | 37.07 | 37.66 | 18.8 | 27.88 | R | 7.1 | 2 |
| Cyg A | Sy 2 | 0.0561 | 44.68 | 44.73 | 4.6e5 | 1.7e6 | 43.81 | 44.17 | 279.8 | 468.6 | R | 9.4 | 11 |
| IGR J20186+4043 | Sy 2 | 0.0144 | 42.57 | 42.98 | < 4.1 | – | < 37.39 | – | – | – | – | – | – |
| 4C 74.26 | Sy 1 | 0.1040 | 44.75 | 45.04 | 190.5 | 208.8 | 41.25 | 41.76 | 259.3 | 1724 | R | 9.6 | 2 |
| S52116+81 | Sy 1 | 0.0840 | 44.25 | 44.77 | 243.8 | 311.6 | 40.71 | 40.99 | 345.6 | 701.6 | R | 8.8 | 2 |
| IGR J21247+5058 | Sy 1 | 0.0200 | 43.81 | 43.96 | 210.6 | 399.6 | 39.51 | 40.47 | 82.28 | 279.3 | R | 6.6 | 1 |
| SWIFT J2127.4+5654 | NLS1 | 0.0140 | 42.89 | 43.04 | 6.0 | 7.3 | 37.53 | 37.62 | < 6.545 | 7.918 | S | 7.2 | 1 |
| RX J2135.9+4728 | Sy 1 | 0.0250 | 43.00 | 43.32 | 6.6 | 7.2 | 38.08 | 38.12 | < 11.69 | < 11.69 | U | – | – |
| NGC 7172 | Sy 2 | 0.0087 | 42.51 | 43.11 | 33.3 | 39.1 | 37.87 | 38.01 | 17.35 | 36.88 | R | 7.7 | 2 |
| MR 2251−178 | Sy 1 | 0.0640 | 44.23 | 44.79 | 15.2 | 17.4 | 39.26 | 39.32 | < 29.92 | < 29.92 | U | 6.9 | 2 |
| MCG−02-58-22 | Sy 1.5 | 0.0469 | 44.16 | 44.25 | 30.8 | 34.8 | 39.29 | 39.35 | < 21.93 | < 21.93 | U | 7.1 | 2 |
| IGR J23308+7120 | Sy 2 | 0.037 | 42.80 | 43.55 | 2.1 | 4.0 | 37.92 | 38.20 | 25 | 40.31 | S | – | – |
| IGR J23524+5842 | Sy 2 | 0.1640 | 44.41 | 44.85 | < 1.5 | – | < 39.06 | – | – | – | – | – | – |

*Notes.* Col. (1) galaxy name; cols (2 and 3) optical classification and redshift from Malizia et al. (2009); cols (4 and 5) 2–10 keV and 20–100 keV logarithmic luminosities in erg s$^{-1}$, corrected for absorption; cols (6 and 7) peak flux density (mJy beam$^{-1}$) and integrated flux density (mJy) at 1.4 GHz; for the SUMSS data the 843 MHz flux has been converted to 1.4 GHz assuming a spectral index of 0.7; cols (8 and 9) 1.4-GHz peak and integrated logarithmic luminosities in erg s$^{-1}$; cols (10 and 11) minor and major axis sizes in kpc measured from the deconvolved sizes at 1.4 GHz from the NVSS and at 843 MHz from the SUMSS; col. (12) radio morphology class, adopting the definitions by Ulvestad & Wilson (1984): 'U' (single, unresolved), 'S' (single, slightly resolved), 'R' (resolved) and 'A' (ambiguous). * source from the SUMSS survey; cols (13 and 14) logarithm of BH mass (in M$_\odot$) and relative reference: (1) Masetti web page: http://www.iasfbo.inaf.it/~masetti/IGR/main.html, (2) Wang, Mao & Wei (2009), (3) Beckmann et al. (2009), (4) Raimundo et al. (2012), (5) Stalin et al. (2011), (6) Perez et al. (1989), (7) Barth et al. (2011), (8) Winter et al. (2009), (9) Kim, Im & Kim (2010), (10) Alonso-Herrero et al. (2013), (11) McKernan, Ford & Reynolds (2010).

$\alpha = 0.7$. This is an average slope value expected for radio optically thin synchrotron emission, however, slopes can vary from steep to flat or inverted depending on the source, usually Seyfert radio cores show flat/inverted slopes on arcsecond scales (Ho & Ulvestad 2001), while steep optically thin synchrotron slopes are associated with extended structures such as lobes. The flux measured can vary by ~30 per cent from steep to flat/inverted slopes during the conversion from 843 MHz to 1.4 GHz; however, this affects only marginally the results on our correlations (see the next section) as the SUMSS sources will probably have spectral slope variously distributed, and these differences will be averaged in the statistical treatment of the fluxes.

The absolute calibration of both the NVSS and SUMSS flux density scale is 3 per cent (Kaplan et al. 1998, uncertainties relative to the Baars et al. 1977 scale).

Following the classification outlined before and adopting definitions consistent with those of Ulvestad & Wilson (1984) and Ho & Ulvestad (2001) for the radio morphology we distinguish between four classes in our sample: 'U' (single, unresolved), 'S' (single, slightly resolved), 'R' (diffuse or linear, clearly resolved) and 'A' (ambiguous, marginally detected). By way of example, in Fig. 1 we show radio images of four galaxies selected as prototype of the different morphological classes proposed, i.e. NGC 5252, NGC 4507, 4C 74.26 and IGR J17513−2011, as U, S, R and A, respectively.

Of the two sources labelled as 'ambiguous', one is only marginally detected (IGR J17513−2011) and one is possibly contaminated by a background radio source (IGR J16185−5928). Note

that also in the NVSS image of IGR J16385−2057, there is a background radio galaxy which might contaminate the radio emission measured; however, this source is still under study and we report it as S (see Tarchi et al. in preparation).

## 4 THE RADIO PROPERTIES OF THE *INTEGRAL* SAMPLE

The complete hard X-ray *INTEGRAL* sample offers the opportunity to study the characteristics of the radio emission at kpc scales for a sample of bright local AGN.

A galaxy was considered detected in the NVSS/SUMSS maps when a source with a peak flux density greater than or equal to three times the rms noise of the map was found coincident, within the uncertainties, with the optical position given in Malizia et al. (2009). Of the 79 sources in this sample, 58 sources belong to the NVSS survey, the remaining 21 have been observed with the SUMSS survey. In our sample, only nine sources have not been detected. We have checked for a possible detection in other observations available in literature and, of the nine undetected sources, only MCG−6-30-15 has been detected with Very Large Array (VLA) at 8.4 GHz with 0.64 mJy (Mundell et al. 2009), while IGR J17488−3253 has an upper limit of 2.1 mJy with GMRT at 0.61 GHz (Pandey et al. 2006), IGR J20186+4043 has been observed with VLA-D and has been associated with an extended radio source, possibility the AGN counterpart, although the association is not secure (Bykov et al. 2006). The remaining sources have no other radio data.
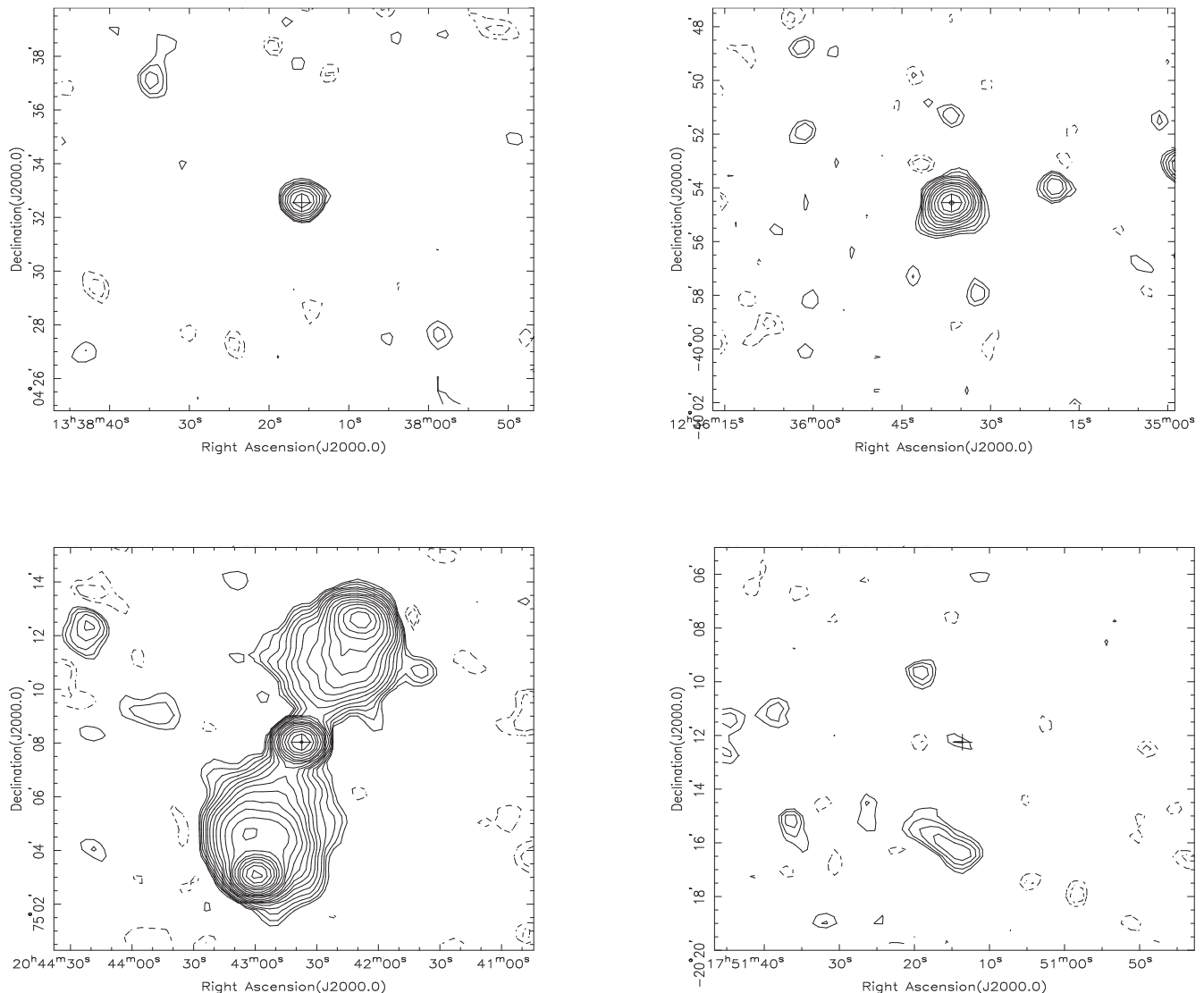
**Figure 1.** Prototype of the different morphological classes proposed, i.e. top left: NGC 5252 (U), top right: NGC 4507 (S), bottom left: 4C 74.26 (R) and bottom right: IGR J17513−2011 (A). The NED optical position is marked with a cross.

Limiting this work to the NVSS and SUMSS observations, the sample detection rate is therefore 89 per cent. This fraction is similar to the 85 per cent found for an optically selected sample observed with VLA (1.4 and 5 GHz) at high resolution (∼1 arcsec) by Ho & Ulvestad ([2001]). The first and only (up to now) radio follow-up of hard X-ray selected sources has been reported in Burlon et al. ([2013]), where only 20 per cent of the *Swift*/BAT AGN are associated with a 20-GHz AT20G detection in the southern sky. However, the low detection rate could be ascribed to the low sensitivity of the AT20G survey (∼40 m Jy) and to the higher observing frequency with respect to the NVSS/SUMSS surveys, suggesting that only bright radio sources are revealed. Indeed, the radio luminosities of Seyfert galaxies in Burlon et al. ([2013]) are almost uniformly distributed from $10^{39}$ to $10^{44}$ erg s$^{-1}$, while *INTEGRAL* sources show 1.4-GHz peak luminosities that vary from ∼$10^{37}$ up to ∼$10^{44}$ erg s$^{-1}$, with a peak distribution around $10^{37}$–$10^{40}$ erg s$^{-1}$. However, *INTEGRAL* AGN are still radio bright when compared with optically selected Seyferts, whose radio luminosities are typi-

cally found in the range $10^{34-42}$ erg s$^{-1}$ (Nagar et al. [2002]; Panessa et al. [2007]).

A measure of the radio brightness with respect to other wavelengths is given by the radio loudness, classically defined by the ratio between the radio and the optical luminosities. Among optically selected AGN, the radio-loudness parameter shows a bimodal distribution dividing radio-loud and radio-quiet AGN at the limit of $R \equiv L_R/L_B \leq 10$ (Kellermann et al. [1989]). Lately, Terashima & Wilson ([2003]) have introduced the X-ray radio-loudness parameter $R_X \equiv L_R/L_{2-10\,\mathrm{keV}}$. Indeed, the X-ray luminosity is ideal to avoid extinction problems which normally occur in the optical band. An even more absorption unbiased measure is given by using the hard X-ray luminosity; therefore, here we define the hard X-ray radio-loudness parameter as $R_{HX} \equiv L_R/L_{20-100\,\mathrm{keV}}$. In Fig. [2], we plot the X-ray and hard X-ray radio-loudness histograms, the blue line shows the radio-loud versus radio-quiet limit set by Terashima & Wilson ([2003]), i.e. $R_X = -4.5$. The *INTEGRAL* sample is characterized both by radio-quiet and radio-loud AGN, with a prevalence of
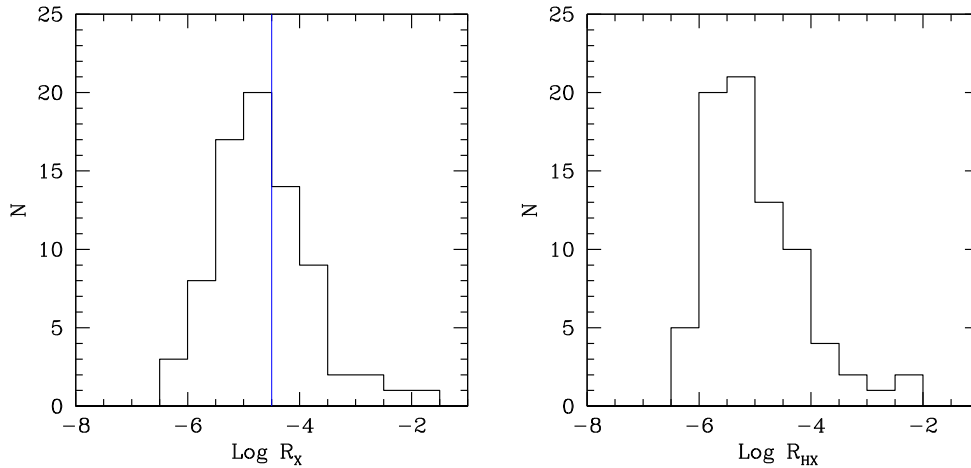
**Figure 2.** Left: X-ray radio loudness given by the ratio of the 1.4-GHz peak luminosity over the 2–10 keV luminosity. The blue line is the radio-loud versus radio-quiet limit set by Terashima & Wilson (2003). Right: hard X-ray radio loudness given by the ratio of the 1.4-GHz peak luminosity over the 20–100 keV luminosity.

radio-quiet AGN; however, the hard X-ray emission is clearly dominant with respect to the radio emission. From a comparison with the radio-loudness distribution in the BAT sample from Burlon et al. (2013), we find that their sources are more radio loud ($-4 < \log R_{HX} < 0$). Again, the high limiting flux density of the AT20G survey allows the detection of only very bright radio sources, while the use of NVSS/SUMSS data allows the detection of low radio luminosity sources also. No bimodality is found in the radio-loudness distribution, in agreement with recent findings that suggest that the bimodality is a consequence of selection biases while well-selected samples of AGN show a continuous level of radio loudness (e.g. Cirasuolo et al. 2003; La Franca et al. 2010).

In our sample, a wide range of radio morphologies is seen. 36 of the 70 objects (51 per cent) detected in the NVSS/SUMSS maps show an unresolved (22) or slightly resolved (14) central source coincident, within the uncertainties, with the position of the optical nucleus. Except for the two 'ambiguous', the remaining 31 sources (44 per cent of all detected objects) show evident extended emission, either 'linear' or 'diffuse', with linear sizes ranging from a few kpc to hundreds of kpc. In particular, sources with 'linear' radio morphology show triple or double emitting structures, thus indicating the presence of large-scale radio jets/lobes, with or without a compact core, respectively, typically found in powerful radio galaxies. Indeed, some of the sources in the sample labelled as 'resolved' (e.g. Cen A and Cyg A) are among the most famous radio galaxies

in the sky. Extended-diffuse morphologies might appear unresolved or slightly resolved sources if the host galaxy is distant enough (for the survey angular resolution). However, in our sample of local galaxies, U, S and R sources are equally distributed in redshift; interestingly, one of the most distant sources, IGR J18249−3243, is one of the most extended ones (see Landi et al. 2009).

## 5 THE X-RAY VERSUS RADIO CORRELATION

We have used the ASURV program (Feigelson & Nelson 1985; Isobe, Feigelson & Nelson 1986) for the statistical analysis of our correlations, which includes several statistical methods that deal with data sets containing both detections and non-detections (upper limits in our case). Within the program, we have used the generalized version of Spearman's rank order correlation coefficient and the generalized Kendall's $\tau$ test to compute the correlation significance. The Buckley–James regression method has been used to calculate the linear regression coefficients. In Table 2, we report the results of the statistical analysis.

In Fig. 3, we show the 1.4-GHz peak (left) and integrated (right) luminosity versus the 20–100 keV luminosity with its best-fitting regression lines. The two correlations are both highly significant (see Table 2) and display a very similar slope (1.21 ± 0.15 and 1.20 ± 0.16, respectively). A similar result is obtained if the radio peak and integrated luminosities are plotted against the 2–10 keV

**Table 2.** The NVSS data for the *INTEGRAL*/IBIS complete sample of AGN.

| Variables (1) | $N$ (2) | Spearman (3) | $p$-value (4) | $z$-score (5) | $p$-value (6) | Partial $\tau$ (7) | $\sigma$ (8) | Prob. (9) | $a$ (10) | $b$ (11) |
|---|---|---|---|---|---|---|---|---|---|---|
| $\log L_{1.4\,\mathrm{GHz\,peak}}$ versus $\log L_{HX}$ | 79 | 0.757 | 0.0 | 7.390 | 0.0 | 0.33 | 0.05 | 0.0 | 1.21 ± 0.15 | −14.0 |
| $\log L_{1.4\,\mathrm{GHz\,int}}$ versus $\log L_{HX}$ | 70 | 0.673 | $1.1 \times 10^{-8}$ | 6.136 | 0.0 | 0.28 | 0.06 | 0.0 | 1.20 ± 0.16 | −13.4 |
| $\log L_{1.4\,\mathrm{GHz\,peak}}$ versus $\log L_{X}$ | 78 | 0.751 | 0.0 | 7.270 | 0.0 | 0.32 | 0.06 | 0.0 | 1.17 ± 0.13 | −12.1 |
| $\log L_{1.4\,\mathrm{GHz\,int}}$ versus $\log L_{X}$ | 70 | 0.658 | $2.3 \times 10^{-8}$ | 5.918 | $1.7 \times 10^{-9}$ | 0.28 | 0.06 | $1.4 \times 10^{-4}$ | 1.08 ± 0.15 | −7.7 |
| $\log F_{1.4\,\mathrm{GHz\,peak}}$ versus $\log F_{HX}$ | 79 | 0.594 | $7.8 \times 10^{-8}$ | 5.581 | $1.2 \times 10^{-8}$ | – | – | – | 1.42 ± 0.26 | −0.6 |
| $\log F_{1.4\,\mathrm{GHz\,peak}}$ versus $\log F_{X}$ | 78 | 0.566 | $3.4 \times 10^{-7}$ | 5.250 | $7.6 \times 10^{-8}$ | – | – | – | 1.03 ± 0.20 | −4.3 |

*Notes.* Cols (2–4): number of variables, Spearman's $\rho$ correlation coefficient and probability for rejecting the null hypothesis that there is no correlation; cols (5 and 6): generalized Kendall's $\tau$ $z$-score and probability for the null hypothesis; cols (7–9): partial Kendall's $\tau$ correlation coefficient, the square root of the variance, $\sigma$, and the associated probability $P$ for the null hypothesis; cols (10 and 11): correlation coefficient of the best-fitting linear regression line calculated using Backley–James linear regression method, $Y = a \times X + b$.
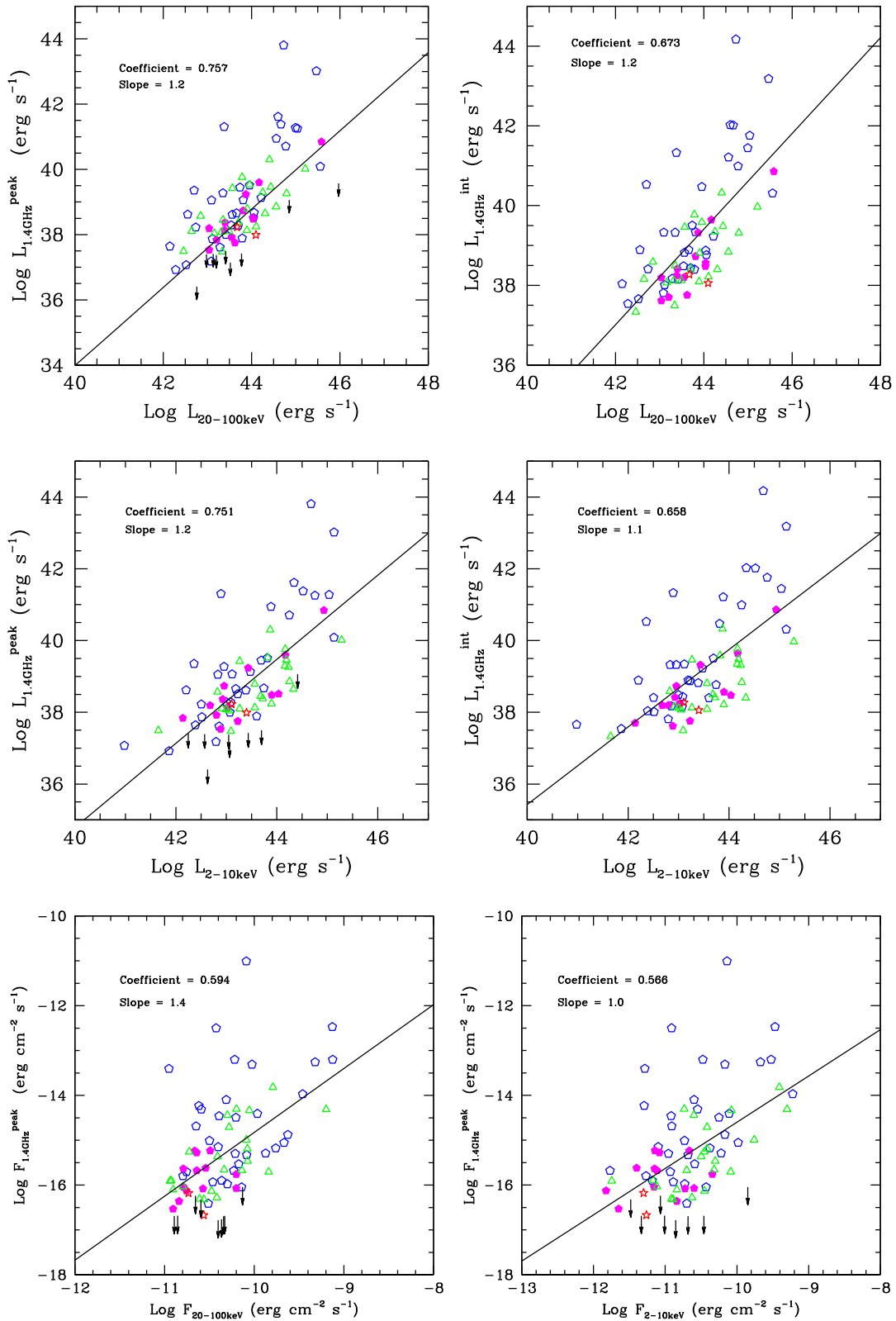
**Figure 3.** Upper panels: 1.4 GHz peak (left) and integrated (right) versus 20–100 keV luminosity. Middle panels: 1.4-GHz peak (left) and integrated (right) versus 2–10 keV luminosity. Bottom panels: 1.4 GHz peak versus 20–100 keV (left) and 2–10 (right) fluxes. The relative best-fitting regression line is shown for each correlation. Different morphological classes are marked as follows: resolved sources (R) are blue empty pentagons, slightly resolved (S) sources are magenta solid pentagons, unresolved (U) sources are green empty triangles, ambiguous (A) sources are red stars. Upper limits are marked as black arrows.

luminosity (Fig. 3), i.e. high significance and correlation slopes of $1.12 \pm 0.13$ and $1.08 \pm 0.15$, consistent within errors. We note that hard X-ray fluxes show typically larger values than the 2–10 keV ones, this naturally yields to a steeper correlation slope.

Luminosity–luminosity correlations may be distance driven. To check for a possible dependence on the distance, we have performed a partial Kendall $\tau$ correlation test, which computes partial correlation coefficient and significance for censored data using three variables, where we took the distance as the third variable (Akritas & Siebert 1996). The partial Kendall's $\tau$ test results (see Table 2) suggest that the correlations are not driven by distance effects. As a further check, we compute the correlation significance for the flux–flux plot of 1.4-GHz peak flux versus 20–100 and 2–10 keV fluxes (Fig. 3) and, despite the large scatter, the correlation remains statistically significant.

We compare our results with those from Burlon et al. (2013), in which the 15–55 keV BAT luminosities are correlated with the 20 GHz ones. As pointed out by the authors, at 20 GHz most of the extended structures are resolved, allowing a more direct comparison between the core radio emission and the hard X-rays. The correlation slope for their Seyfert sample is log $L_{15-55\,\text{keV}} \propto 0.7$ log $L_{20\,\text{GHz}}$, slightly steeper but in agreement within errors with the values found in our sample; however, the weak correlation found is clearly driven by distance effects, in fact their sample is characterized by several sources at high $z$.

## 6 DISCUSSION

In BH systems, the X-ray emission typically originates in the accretion flow surrounded by a hot corona or alternatively at the base of a jet (Markoff, Nowak & Wilms 2005). The radio emission is associated with the presence of a jet of relativistic particles emitting synchrotron radiation at radio frequencies. AGN with powerful relativistic jets only makes up 10–20 per cent of the entire AGN population (Kellermann et al. 1989), the majority of which is instead quiet in the radio, although not silent (Ho & Ulvestad 2001). Radio cores are almost ubiquitously observed depending on the survey flux limit and frequency. The 89 per cent detection rate of radio sources found within the *INTEGRAL* AGN survey is in agreement with these previous statements.

The existence of a relation between the X-ray and the radio emission in both stellar and supermassive BHs has opened new scenarios on the comprehension of the accretion–ejection mechanisms (Corbel et al. 2003; Gallo et al. 2003; Merloni et al. 2003; Falcke et al. 2004). Stellar-mass BHs follow a standard relation $L_R \propto L_X^{0.5-0.7}$ when they are found in their soft state (Corbel et al. 2003; Gallo et al. 2003). Interestingly, the Fundamental Plane, which unifies XRBs and AGN by scaling the radio and X-ray luminosity with the BH mass, displays the same slope (Merloni et al. 2003). For these classes of sources it has been proposed that an inefficient accretion flow model coupled with a (scale invariant) jet can reproduce the observed slope. Indeed, when the disc accretes at radiatively inefficient regime, the advected flow plus jet can explain both the X-ray and radio emission (e.g. Narayan & Yi 1994).

Since the discovery of the original correlation, more and more outliers to the standard correlation are found, i.e. for a given X-ray luminosity the radio emission is fainter resulting in steeper slopes (e.g. Soleri et al. 2010). Coriat et al. (2011) propose that, assuming a standard emission model of compact jets, the steeper relation (∼1.4) implies that the accretion flow is radiatively efficient, where the limit for the transition between radiatively inefficient and radiatively efficient is set to an X-ray luminosity higher than
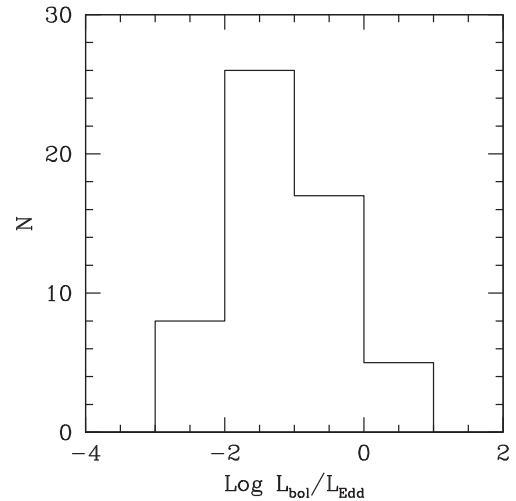


**Figure 4.** Distribution of the log Eddington ratio defined as the logarithm of the ratio between the bolometric luminosity and the Eddington luminosity, $L_{\text{bol}}/L_{\text{Edd}}$.

$5 \times 10^{-3} L_{\text{Edd}}$. Dong et al. (2014) have confirmed this hypothesis for a sample of high Eddington ratio AGN, by assuming $L_R \propto Q_{\text{jet}}^{1.4} \propto \dot{M}^{1.4}$. The significant correlation found for the *INTEGRAL* AGN sample confirms these previous works. The 1.4 GHz versus 20–100 keV emission correlates with a slope of $1.2 \pm 0.15$, steeper than the classical 0.5–0.7, and consistent within errors with the expected 1.4. Indeed, the Eddington ratios ($L_{\text{bol}}/L_{\text{Edd}} \geq 10^{-3}$, where the bolometric luminosity is derived by applying a correction factor of 20 to the 2–10 keV luminosity; see Vasudevan & Fabian 2007) of the *INTEGRAL* sample (see Fig. 4) strongly suggest that these sources are efficient accreting systems, as expected from their hard X-ray selection, and behave like the outliers XRB systems discussed by Coriat et al. (2011). All the above-mentioned theoretical considerations assume a standard behaviour for the jet and ascribe the observed correlation slope to a particular accretion regime; however, the jet emission depends on several parameters: a change in one of those (e.g. the magnetic field) could modify the radio output with strong influence in the correlation slope (see the discussion in Coriat et al. 2011).

We note that the radio data presented here comprise the emission over kpc scale extension. At intermediate radio resolutions (such as those of the VLA-A observation, i.e. arcsec), the emission comes from pc scales and the X-ray emission still correlates with the radio emission at 1.4, 5 and 15 GHz (Panessa et al. 2007), with a similar level of significance. However, at very long baseline interferometry scales (milliarcsec), no correlation is found for a sample of Seyfert galaxies, suggesting that the very inner radio core emission at sub-pc scales is not related to the X-rays (Panessa & Giroletti 2013). All these pieces of evidence support the idea that the disc–corona emission correlates with the total radio emission, rather than with the inner jet emission.

However, all the above-mentioned works cannot rely on the simultaneity of the radio versus X-ray data. When simultaneous data are taken, only very weak correlations are found (Jones et al. 2011; King et al. 2011, 2013). For both nearby AGN NGC 4051 and NGC 4395, the intrinsic X-ray variability is observed to be stronger than the radio variability. Assuming that the corona is at the base of a jet, the X-ray variations may be filtered by the corona and only partially transferred to the jet. However in these works, radio data are at arcsec scales, implying that the radio emission is averaged on

a few hundreds pc, the different X-ray versus radio spatial scales sampled could explain the different variability. Interestingly, the simultaneous $L_R \propto L_X$ slopes are steeper (around unity) than the standard 0.6, suggesting that these sources are X-ray bright and that their emission is accretion dominated.

In interpreting the X-rays and hard X-rays versus 1.4 GHz correlations with our data sets we should consider two more important aspects. One is that the lower the radio frequency is, the more the emission is contaminated by diffuse components, such as lobes on a few kpc to hundreds of kpc spatial scales. This implies that the time-scales sampled by the NVSS and SUMSS surveys vary over thousands of years, i.e. the time needed by electrons to propagate into the medium. On the other hand, the X-ray flux is averaged over tens of ks observations (few days), while the *INTEGRAL* hard X-ray emission is averaged over months to several years of sky surveying. Both the X-ray and hard X-ray emission are produced within the inner region of the accretion flow (inner disc–corona); therefore, the X-ray spatial scale sampled is of a few gravitational radii. Summarizing, the radio emission is averaged on much larger spatial and time-scales with respect to the X-ray and hard X-ray emission. As a consequence, the present correlations suggest that the accretion-related X-ray emission is related to the diffuse/total radio emission emitted over larger scales. Within our group, we are developing a model which correlates the hard X-ray emission with the total radio emission assuming a more or less spherical bubble on scales of several arc minutes, fed by jets issuing from the core (see Wagner & Bicknell 2011; Wagner, Bicknell & Umemura 2012). Details on this theoretical treatment and interpretation of the X-ray/radio correlations examined here and its implications will be presented and discussed in a future work (Bicknell et al. in preparation).

## 7 CONCLUSION

We have selected a complete sample of hard X-ray AGN from the *INTEGRAL* survey in order to study the relation between the X-ray and hard X-ray emission with the radio emission in a sample of bright sources. First, we have analysed the radio images from the NVSS and SUMSS surveys detecting a large fraction of sources (89 per cent), with different morphologies, from unresolved/slightly resolved to extended sources over hundreds of kpc scales. We find the existence of a significant correlation between the X-ray and hard X-ray luminosities and the peak and integrated 1.4-GHz radio luminosities. Correlation slopes are around 1–1.2, clearly steeper than the classical 0.6 value found in the Fundamental Plane for BH activity and consistent with the 1.4 expected for sources belonging to the efficient accretion branch (Coriat et al. 2011; Dong et al. 2014). This suggests that the *INTEGRAL* AGN are X-ray-dominated (accretion dominated) sources accreting at high Eddington ratios and the high-energy emission from the central engine is related to the radio emission averaged over kpc scales (i.e. thousands of years).

## ACKNOWLEDGEMENTS

## REFERENCES

Akritas M. G., Siebert J., 1996, MNRAS, 278, 919
Alonso-Herrero A., Pereira-Santaella M., Rieke G. H., Diamond-Stanic A. M., Wang Y., Hernán-Caballero A., Rigopoulou D., 2013, ApJ, 765, 78
Baars J. W. M., Genzel R., Pauliny-Toth I. I. K., Witzel A., 1977, A&A, 61, 99
Barth A. J. et al., 2011, ApJ, 743, L4
Beckmann V. et al., 2009, A&A, 505, 417
Bird A. J. et al., 2007, ApJS, 170, 175
Bird A. J. et al., 2010, ApJS, 186, 1
Bock D. C.-J., Large M. I., Sadler E. M., 1999, AJ, 117, 1578
Bonchi A., La Franca F., Melini G., Bongiorno A., Fiore F., 2013, MNRAS, 429, 1970
Brinkmann W., Laurent-Muehleisen S. A., Voges W., Siebert J., Becker R. H., Brotherton M. S., White R. L., Gregg M. D., 2000, A&A, 356, 445
Burlon D., Ajello M., Greiner J., Comastri A., Merloni A., Gehrels N., 2011, ApJ, 728, 58
Burlon D., Ghirlanda G., Murphy T., Chhetri R., Sadler E., Ajello M., 2013, MNRAS, 431, 2471
Bykov A. M. et al., 2006, ApJ, 649, L21
Canosa C. M., Worrall D. M., Hardcastle M. J., Birkinshaw M., 1999, MNRAS, 310, 30
Cao X.-F., Wu Q., Dong A.-J., 2014, ApJ, 788, 52
Cattaneo A., Dekel A., Devriendt J., Guiderdoni B., Blaizot J., 2006, MNRAS, 370, 1651
Cattaneo A. et al., 2009, Nature, 460, 213
Cirasuolo M., Magliocchetti M., Celotti A., Danese L., 2003, MNRAS, 341, 993
Condon J. J., Cotton W. D., Greisen E. W., Yin Q. F., Perley R. A., Taylor G. B., Broderick J. J., 1998, AJ, 115, 1693
Corbel S., Nowak M. A., Fender R. P., Tzioumis A. K., Markoff S., 2003, A&A, 400, 1007
Coriat M. et al., 2011, MNRAS, 414, 677
Croton D. J. et al., 2006, MNRAS, 365, 11
Dong A.-J., Wu Q., Cao X.-F., 2014, ApJ, 787, L20
Falcke H., Körding E., Markoff S., 2004, A&A, 414, 895
Feigelson E. D., Nelson P. I., 1985, ApJ, 293, 192
Gallo E., Fender R. P., Pooley G. G., 2003, MNRAS, 344, 60
Ho L. C., Ulvestad J. S., 2001, ApJS, 133, 77
Isobe T., Feigelson E. D., Nelson P. I., 1986, ApJ, 306, 490
Iwasawa K., Fabian A. C., Matt G., 1997, MNRAS, 289, 443
Jarosik N. et al., 2011, ApJS, 192, 14
Jones S., McHardy I., Moss D., Seymour N., Breedt E., Uttley P., Körding E., Tudose V., 2011, MNRAS, 412, 2641
Kaplan D. L., Condon J. J., Arzoumanian Z., Cordes J. M., 1998, ApJS, 119, 75
Kellermann K. I., Sramek R., Schmidt M., Shaffer D. B., Green R., 1989, AJ, 98, 1195
Kim D., Im M., Kim M., 2010, ApJ, 724, 386
King A. L. et al., 2011, ApJ, 729, 19
King A. L., Miller J. M., Reynolds M. T., Gültekin K., Gallo E., Maitra D., 2013, ApJ, 774, L25
La Franca F., Melini G., Fiore F., 2010, ApJ, 718, 368
Landi R. et al., 2009, A&A, 493, 893
McKernan B., Ford K. E. S., Reynolds C. S., 2010, MNRAS, 407, 2399
Malizia A., Stephen J. B., Bassani L., Bird A. J., Panessa F., Ubertini P., 2009, MNRAS, 399, 944
Markoff S., Nowak M. A., Wilms J., 2005, ApJ, 635, 1203
Marulli F., Bonoli S., Branchini E., Moscardini L., Springel V., 2008, MNRAS, 385, 1846
Matt G., Bianchi S., Guainazzi M., Molendi S., 2004, A&A, 414, 155
Mauch T., Murphy T., Buttery H. J., Curran J., Hunstead R. W., Piestrzynski B., Robertson J. G., Sadler E. M., 2003, MNRAS, 342, 1117
Merloni A., Heinz S., di Matteo T., 2003, MNRAS, 345, 1057
Mundell C. G., Ferruit P., Nagar N., Wilson A. S., 2009, ApJ, 703, 802

Nagar N. M., Falcke H., Wilson A. S., Ulvestad J. S., 2002, A&A, 392, 53

Narayan R., Yi I., 1994, ApJ, 428, L13

Pandey M., Rao A. P., Manchanda R., Durouchoux P., Ishwara-Chandra C. H., 2006, A&A, 453, 83

Panessa F., Giroletti M., 2013, MNRAS, 432, 1138

Panessa F., Barcons X., Bassani L., Cappi M., Carrera F. J., Ho L. C., Pellegrini S., 2007, A&A, 467, 519

Perez E., Manchado A., Garcia-Lario P., Pottasch S. R., 1989, A&A, 215, 262

Raimundo S. I., Fabian A. C., Vasudevan R. V., Gandhi P., Wu J., 2012, MNRAS, 419, 2529

Schmidt M., 1968, ApJ, 151, 393

Soleri P. et al., 2010, MNRAS, 406, 1471

Stalin C. S., Jeyakumar S., Coziol R., Pawase R. S., Thakur S. S., 2011, MNRAS, 416, 225

Terashima Y., Wilson A. S., 2003, ApJ, 583, 145

Ulvestad J. S., Wilson A. S., 1984, ApJ, 285, 439

Vasudevan R. V., Fabian A. C., 2007, MNRAS, 381, 1235

Wagner A. Y., Bicknell G. V., 2011, ApJ, 728, 29

Wagner A. Y., Bicknell G. V., Umemura M., 2012, ApJ, 757, 136

Wang J., Mao Y. F., Wei J. Y., 2009, AJ, 137, 3388

Winter L. M., Mushotzky R. F., Reynolds C. S., Tueller J., 2009, ApJ, 690, 1322

This paper has been typeset from a TEX/LATEX file prepared by the author.